Nanoscale Horizons

ROYAL SOCIETY OF CHEMISTRY

COMMUNICATION

View Article Online
View Journal

Cite this: DOI: 10.1039/d5nh00306g

Received 3rd May 2025,
Accepted 9th October 2025

DOI: 10.1039/d5nh00306g

rsc.li/nanoscale-horizons

Synthesis of carbon nanocomposites consisting of nanocellulose-derived carbon and reduced graphene oxide for high-performance captive deionization

Azhar Alowasheeir, †[a] Md. Ikram Ul Hoque, †[bc] Xingtao Xu, [d] Scott W. Donne, [c] Yoshio Bando, [efg] Saad M. Alshehri, [f] Tansir Ahamad, [f] Md Shahriar A. Hossain, [be] Yusuke Yamauchi, [abh] Nasim Amiralian, *[b] Dong Jiang*[ab] and Yusuke Asakura *[a]

Several types of nanocellulose-derived carbon/reduced graphene oxide (rGO) nanocomposites are synthesized using three nanocellulose types: cellulose nanofibers (CNF), long cellulose nanocrystals (CNC-L), and short cellulose nanocrystals (CNC-S). The nanocomposites achieve a large surface area due to the small nanocellulose fibers acting as spacers. For the capacitive deionization (CDI) test, the CNC-L/rGO is selected and compared with the rGO prepared without nanocelluloses. It achieves a high sodium ion adsorption capacity of 45.67 mg g^{-1} and a high salt adsorption capacity of 57.08 mg g^{-1} at a NaCl concentration of 2000 mg L^{-1}. Excellent stability and performance are also confirmed across varying saline concentrations. These outstanding properties make the CNC-L/rGO a promising electrode material for efficient and sustainable water desalination.

New concepts

Capacitive deionization (CDI) is a promising desalination technology due to its low energy consumption and eco-friendly nature. However, the performance of CDI electrodes remains a critical challenge, particularly in achieving high salt adsorption capacity, fast ion transport, and long-term cycling stability. In this study, we introduce a new class of nanocomposites derived from nanocellulose and reduced graphene oxide (rGO), where nanocellulose functions as a structural spacer to prevent rGO restacking and enhance pore accessibility. By employing three distinct nanocellulose morphologies—cellulose nanofibers (CNF), long cellulose nanocrystals (CNC-L), and short cellulose nanocrystals (CNC-S)—we systematically control the structure and porosity of the resulting composites. Among these, CNC-L/rGO delivers an exceptional CDI performance, achieving a Na^+ adsorption capacity of 45.67 mg g^{-1} and outstanding cycling durability. This work represents the first application of nanocellulose-derived carbon/rGO nanocomposites for CDI, offering a sustainable and tunable material platform. The strategic integration of renewable nanocellulose with conductive carbon architectures opens a new avenue in designing high-performance CDI electrodes. These findings not only advance the understanding of hierarchical carbon composite design but also offer practical insight for scalable desalination technologies targeting freshwater scarcity.

1. Introduction

Freshwater scarcity, a pressing global challenge exacerbated by climate change, overpopulation, water pollution, and unsustainable water resource utilization, demands innovative solutions.[1,2] Desalination, the process of removing salts from saltwater or brackish water, presents a promising avenue for producing clean, fresh water. There are several desalination methods, such as thermal desalination and membrane-based techniques. Thermal desalination utilizes heat to evaporate water and separate it from salts, while membrane-based techniques, such as reverse osmosis and electrodialysis, employ semi-permeable membranes to filter out salts.[1,3] In these desalination processes, however, high energy consumption, substantial costs, and potential environmental impacts pose

[a] Department of Materials Process Engineering, Graduate School of Engineering, Nagoya University, Nagoya 464-8603, Japan. E-mail: dongjiang@toki.waseda.jp, asa.y@nagoya-u.jp
[b] Australian Institute for Bioengineering and Nanotechnology (AIBN), The University of Queensland, Brisbane, Queensland 4072, Australia. E-mail: n.amiralian@uq.edu.au
[c] Discipline of Chemistry, The University of Newcastle, University Drive, Callaghan, NSW 2308, Australia
[d] Marine Science and Technology College, Zhejiang Ocean University, Zhoushan, China
[e] School of Mechanical and Mining Engineering, Faculty of Engineering, Architecture, and Information Technology (EAIT), The University of Queensland, Brisbane, QLD, 4072, Australia
[f] Chemistry Department, College of Science, King Saud University, Riyadh 11451, Saudi Arabia
[g] Australian Institute for Innovative Materials, University of Wollongong, North Wollongong 2500, Australia
[h] Department of Chemical and Biomolecular Engineering, Yonsei University, 50 Yonsei-ro, Seodaemun-gu, Seoul 03722, South Korea
† These authors contributed equally to this work.

limitations for large-scale freshwater production.[4–6] Recently, capacitive deionization (CDI) has garnered significant interest among researchers worldwide.[1,2,4,7–9] The CDI operates at a low voltage between two electrodes, where ions from an aqueous solution are adsorbed *via* the electrical double layer (EDL) mechanism. This process does not generate harmful byproducts. Instead, energy can be recovered during the release of counter ions and electrode regeneration by simply reversing the electrode polarity. Consequently, CDI is considered a promising desalination technology due to its cost-effectiveness, high energy efficiency, and environmentally friendly attributes compared to conventional desalination methods.

The efficiency and capacity of CDI technology are strongly dependent on the electrode properties. To date, a wide range of nanoporous materials, including carbon-based materials, metal–organic frameworks (MOFs), covalent-organic frameworks (COFs),[10] polymers, and metal oxides,[11] have been investigated for CDI applications.[1,2,8,12–14] Among these, carbon-based materials, such as carbon aerogels,[15] activated carbon,[16] carbon nanotubes (CNTs)-based composites,[17] nanostructured carbon[18] and other graphene-based materials,[19] are favored due to their desirable properties, including high electrical conductivity, good chemical stability, and ease of surface modification, coupled with economic benefits such as low synthesis cost and abundance.[1,12] The CDI's electrochemical functions, mechanisms, and principles are closely related to those of supercapacitors. Therefore, physicochemical parameters that enhance supercapacitor performance are similarly effective in the CDI.[1,12,20,21]

Graphene-based nanocomposites have shown promise in various electrochemical applications.[22,23] Graphene plays a vital role in these nanocomposites, enhancing electrical conductivity and physicochemical stability. However, graphene nanosheets themselves are seriously stacked to each other, reducing the exposed active surface area. Self-assembly of graphene nanosheets can yield porous nanoarchitecture by incorporating with CNTs or crosslinking with polymers.[19] Nanocelluloses that can be widely obtained from natural cellulose sources exhibit one-dimensional (1D) morphologies having uniform diameters ranging from 10–100 nm and lengths from 100 nm to several microns.[22–25] By using different types of nanocelluloses, carbon materials with varying morphologies, textures, *etc.*, can be designed in a desired manner.[22,23,26] Therefore, graphene-based nanocomposites with nanocelluloses as spacers are expected to retain high exposed surface area, and they are expected to be a promising candidate for CDI applications. To the best of our knowledge, however, the application of nanocellulose-derived carbon/rGO nanocomposites to CDI has not been previously reported. In this study, we report the synthesis of nanocellulose-derived carbon/rGO nanocomposites using three types of nanocellulose produced *via* different treatments, each exhibiting unique distinctions in morphologies, size, and properties: (1) CNF (cellulose nanofibril) with a width of 2–50 nm and a length of 1–3 μm (the most extended length among the types), (2) CNC-L (long cellulose nanocrystal) with a width of 10–20 nm and a length of 500–1000 nm (shorter than CNF but longer than CNC-S), and (3) CNC-S (short cellulose nanocrystal) with a width of 10–20 nm and a length of 300–500 nm (the shortest length) (Scheme 1). Importantly, in this design, nanocellulose acts not only as a spacer but also as a morphology-regulating agent. Specifically, differences in fiber length and crystallinity among CNF, CNC-L, and CNC-S allow for precise tuning of the resulting pore architectures and conductive pathways. The CNC-L forms an extended conductive network and introduces a larger mesoporous structure, while the CNC-S forms a denser and more compact structure. This structural tunability allows for effective control over ion transport dynamics in the CDI system.[27] Furthermore, the incorporation of appropriately-sized nanocellulose spacers suppresses the restacking of the rGO layers and enhances ion accessibility.[28]

In parallel, recent studies have emphasized the importance of architecturally-engineered electrodes that integrate hierarchical porosity, structural stability, and well-defined ion transport pathways to advance CDI performance.[29] Our design strategy is well aligned with this emerging direction. The concept of using bio-derived nanoscale spacers to regulate the structure of two-dimensional materials can be extended to other layered materials such as MXenes, layered double hydroxides, and transition metal dichalcogenides. We comprehensively characterize the resulting nanocomposites to determine their physicochemical properties, including morphologies, textures, surface areas, pore size distributions, *etc.* The synthesized nanocomposites are then used to fabricate electrodes for a CDI device under controlled conditions (Fig. S1), enabling us to systematically study and evaluate the impact of nanocelluloses on the CDI performance. Our nanocomposite demonstrates remarkable performance in the CDI applications in comparison with rGO prepared without nanocelluloses, underscoring their potential as highly efficient materials for water desalination.

Yusuke Yamauchi

Our group has published more than five papers in Nanoscale Horizons, and we are proud to have such a long history of cooperation with this excellent journal. We believe that the most meaningful way to show our appreciation is to continue reporting our significant research advances—such as the second generation of mesoporous materials with unprecedented properties, particularly those involving mobility-controlled electrons beyond MOFs. We look forward to further contributing to this journal. Congratulations on the 10th anniversary, and best wishes to Nanoscale Horizons for continued success.

2. Results and discussion

The preparation process of the nanocellulose-derived carbon/rGO nanocomposites is illustrated in Scheme 1. The GO nanosheet precursor, synthesized using Hummers' method, exhibited a 2D crumpled sheet-like structure. Nanocelluloses

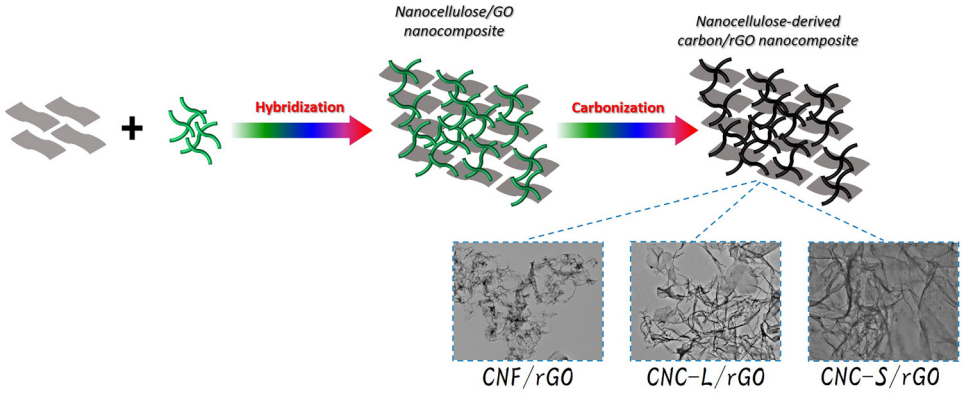

Scheme 1 Synthesis strategy of nanocellulose-derived carbon/rGO nanocomposites prepared with graphene oxide (GO) sheets and nanocellulose as the starting precursors.

were incorporated into this structure through a self-assembly approach, facilitated by the functional groups present on both GO and nanocellulose surfaces (*e.g.*, C–O, C═O, and hydroxyl (–OH) groups).[23,25] These functional groups promoted interactions through ionic interactions and/or hydrogen bonding. The precursor mixture, a brownish-black nanocellulose/GO nanocomposite, was obtained by flash freezing the suspension in liquid nitrogen, followed by drying at low pressure using a freeze dryer. Finally, the powder was carbonized under nitrogen flow at 600 °C for 8 hours to produce the nanocellulose-derived carbon/rGO nanocomposites.

The three different types of nanocellulose used in this study are shown in TEM images in Fig. S2. CNF (Fig. S2a) is produced *via* the mechanical treatment of sugarcane bleached pulp through a high-pressure homogenizer. They consist of a combination of high-aspect-ratio individual fibers and their bundles. The surface of these fibers is rich in hydroxyl groups, which bond through van der Waals forces, causing cellulose chains to stack and form elementary fibrils or nanofibrils.[30–32] CNC-L, derived from sugarcane bleached pulps mild sulfuric acid treatment, also shows an elongated, flexible structure but with shorter fiber lengths (Fig. S2b).[30,33] Negatively charged sulfate groups ($-OSO_3^-$) are introduced onto the CNC's surface, which promotes CNC's dispersion by electrostatic repulsion due to the negative charge.[34] In contrast, CNC-S, obtained from the treatment of wood pulp with sulfuric acid, features rod-shaped cellulose nanocrystals with an average particle length of 291 ± 24 nm and a diameter ranging below 10 nm (Fig. S2c).[35] The morphology

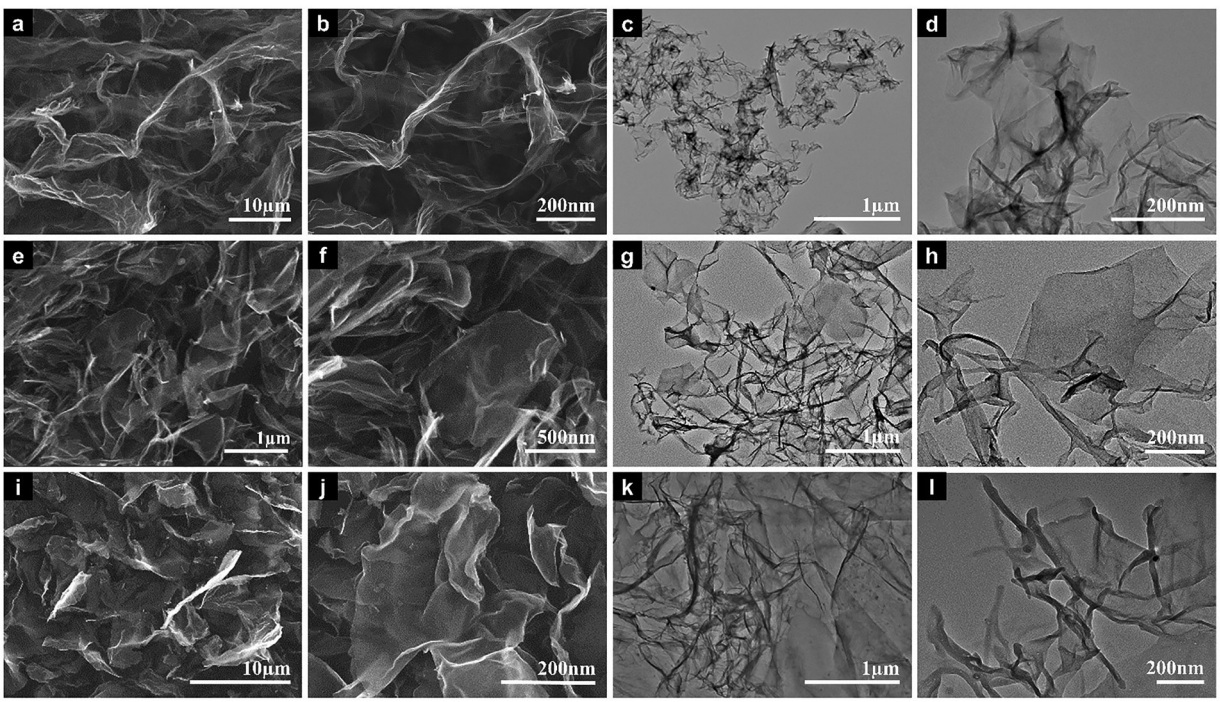

Fig. 1 (a) and (b) SEM and (c) and (d) TEM images of CNF/rGO nanocomposite. (e) and (f) SEM and (g) and (h) TEM images of CNC-L/rGO nanocomposite, and (i) and (j) SEM and (k) and (l) TEM images of CNC-S/rGO nanocomposite.

of rGO is shown in Fig. S3a and b, where the SEM and TEM images display a uniform surface with fewer visible wrinkles.

The above nanocelluloses were combined with GO and calcined at 600 °C to produce carbon nanocomposites. SEM and TEM images (Fig. 1) reveal distinct structural features for each nanocellulose type within the rGO framework. The SEM images (Fig. 1a, b, e, f, i, and j) demonstrate a predominantly sheet-like morphology for all samples, with nanocellulose components blending into the rGO matrix, making it difficult to distinguish between them as only rGO sheets are visible. TEM images at both high and low magnifications illustrate significant differences in nanocellulose morphology and distribution within the rGO composites, impacting the overall structure. In the CNF/rGO composite (Fig. 1c and d), the low magnification TEM clearly reveals the CNF structure, while the high magnification shows CNF encased by thin rGO sheets. For the CNC-L/rGO composite (Fig. 1g–h), low magnification TEM indicates an uneven dispersion of CNC-L and rGO, leading to visible voids and gaps. By contrast, the CNC-S/rGO composite (Fig. 1k–l) displays a compact structure, where CNC-S particles are evenly distributed within the rGO matrix, minimizing voids or large pores.

XRD analysis was conducted to investigate the crystal structure of the materials. Fig. S3c of the rGO XRD pattern exhibits a distinct diffraction peak at 2θ = 26.4° (d-spacing = 0.34 nm) corresponding to the (002) plane. This peak is observed, whereas the characteristic diffraction peak of GO at approximately 11° (d-spacing = 0.81 nm) is not present, indicating the elimination of oxygen-containing functional groups and interlayer water molecules, and confirming the successful conversion of GO to rGO.[36–40] For the CNF/rGO, CNC-L/rGO, and CNC-S/rGO nanocomposites (Fig. 2), XRD peaks appear around 2θ = 26.4°, 26.2°, and 26.4°, respectively, corresponding to the (002) plane where the characteristic peaks of nanocelluloses at 2θ = 15° and 22° disappear following hybridization.[30,36] The observed d-spacing (around 0.34 nm) in all the nanocomposites is consistent with that of rGO without nanocelluloses,[41,42] likely due to the relatively low nanocellulose concentration in the nanocomposite.[42]

Raman spectroscopy is an essential technique for determining the degree of graphitization in carbon-based materials. The number of structural defects is typically assessed by analyzing the intensity ratio of the G band, which corresponds to the graphitic structure with sp^2 hybridization arranged in a two-dimensional lattice, to the D band, which is associated with the presence of amorphous carbon in the sample. The D band typically arises from defects such as boundaries and edges in the carbon lattice.[43] Fig. 3 shows the G and D bands of rGO observed at 1586.4 and 1353.6 cm^{-1}, respectively. The integrated intensity ratio of the D peak to the G peak (I_D/I_G), which indicates the degree of defects in the synthesized materials, is found to be 0.90 for rGO. After hybridization with nanocellulose, the I_D/I_G ratios were calculated to be 0.82, 0.98, and 0.87 for CNF/rGO, CNC-L/rGO, and CNC-S/rGO, respectively. The I_D/I_G ratio of CNC-L/rGO is higher than that of rGO, indicating increased defects or disorders. This is attributed to the observation that CNC-L exhibits the highest degree of amorphous carbon formation during heating at high temperatures.[44]

The thermal stability of GO, CNF/GO, CNC-L/GO, and CNC-S/GO was analyzed using thermogravimetric analysis (TGA) under a nitrogen atmosphere (Fig. 4). The GO (Fig. 4a) exhibits

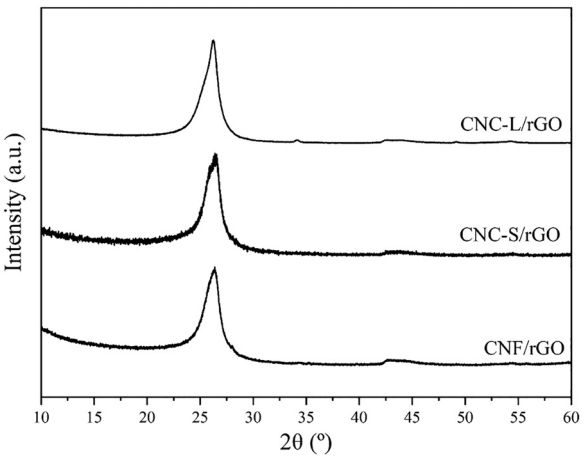

Fig. 2 XRD patterns of CNF/rGO, CNC-L/rGO, and CNC-S/rGO.

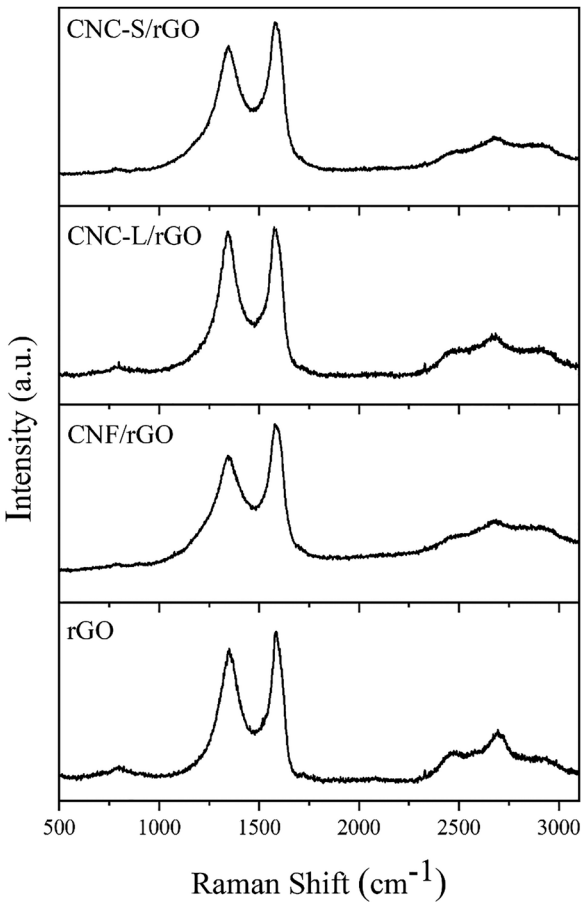

Fig. 3 Raman spectra of rGO, CNF/rGO, CNC-L/rGO, and CNC-S/rGO.

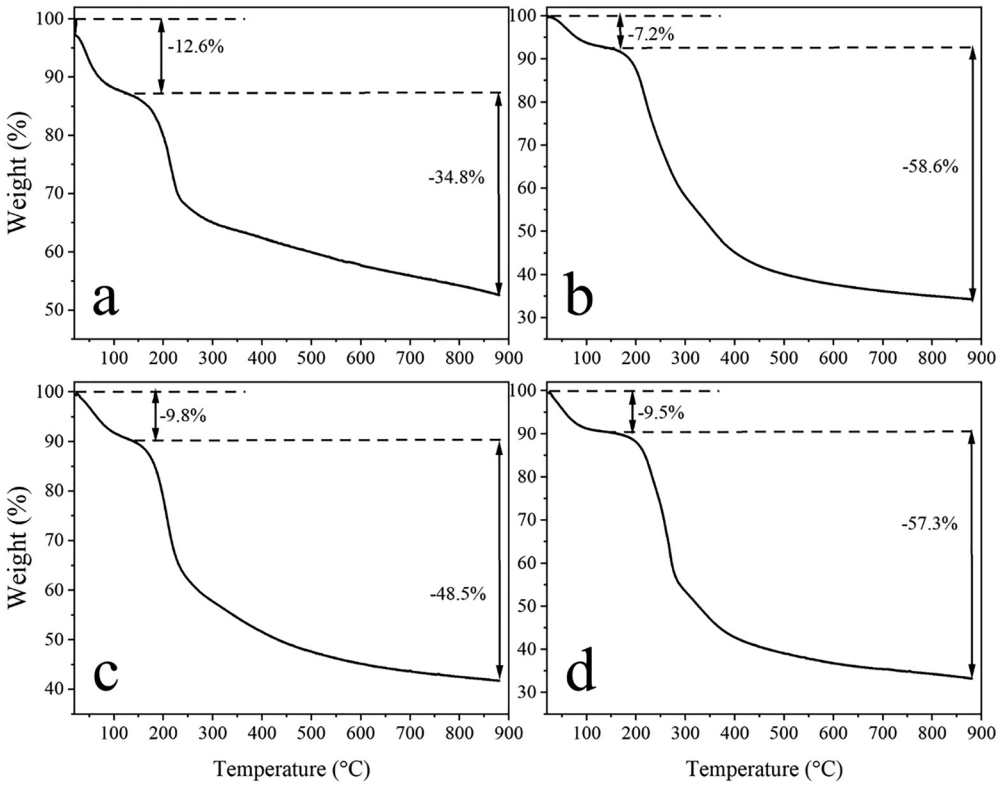

Fig. 4 TGA curves of (a) GO, (b) CNF/GO, (c) CNC-L/GO, and (d) CNC-S/GO under nitrogen flow.

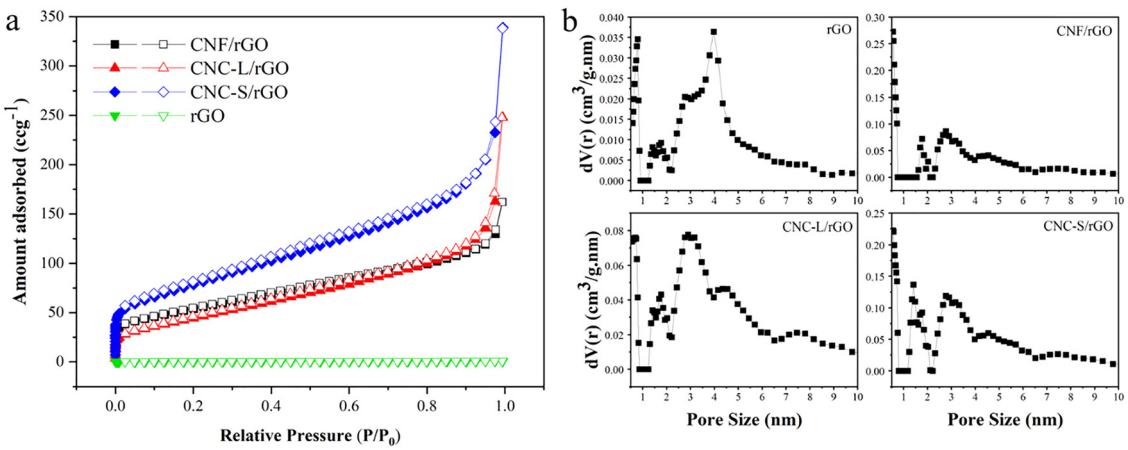

Fig. 5 (a) N_2 adsorption–desorption isotherms, and (b) the NLDFT pore size distribution curves of rGO, CNF/rGO, CNC-L/rGO and CNC-S/rGO.

an initial weight loss of approximately 12.6% below 150 °C due to absorbed water.[45,46] This is followed by a major decomposition of oxygen-containing functional groups with a weight loss of 34.8% up to 880 °C,[47] resulting in a residual weight of 52.6%, which indicates the presence of thermally stable carbonaceous structures. In contrast, the nanocellulose/GO nanocomposites (Fig. 4b–d) also show an initial weight loss below 150 °C related to water adsorption. When carbon yields are calculated by using the weight ratios after water desorption at 150 °C (W [%]) and the residual weight ratios after heating up to 880 °C (R [%]) (Carbonization degree = $W/R \times 100$ [%]), CNC-L/GO exhibits a larger carbon yield (46.2%) compared to CNF/GO (36.9%) and CNC-S/GO (36.7%). The relatively high carbon yield of CNC-L/GO is probably due to strong interactions between CNC-L and the GO matrix.[45]

The surface area and pore size distribution for all nanocellulose-derived carbon/rGO nanocomposites were assessed through nitrogen adsorption/desorption using Brunauer–Emmett–Teller (BET) analysis (Fig. 5a and Table 1). The addition of nanocellulose significantly enhances the surface area of rGO

Table 1 Surface area and pore size of the samples

Sample name	Surface area ($m^2\ g^{-1}$)	Pore volume ($cm^3\ g^{-1}$)
rGO	45.7	0.05
CNF/rGO nanocomposite	188.9	0.18
CNC-L/rGO nanocomposite	170.6	0.23
CNC-S/rGO nanocomposite	283.9	0.33

alone (45.7 $m^2\ g^{-1}$). Precisely, the CNC-S/rGO nanocomposite displays the highest surface area at 283.9 $m^2\ g^{-1}$, followed by CNF/rGO at 188.9 $m^2\ g^{-1}$ and CNC-L/rGO at 170.6 $m^2\ g^{-1}$. This increase is likely due to the small nanocellulose fibers acting as spacers, which help prevent rGO sheets from restacking and maintain their separation. Fig. 5b shows the pore size distributions of the samples. The distributions indicate mesopores are largely introduced by hybridization.

Numerous studies have demonstrated that the presence of relatively large pores like mesopores is a critical factor in the design and performance of CDI materials, as it significantly influences the ability of electrode materials to store and release ions.[48,49] CNF/rGO, CNC-L/rGO, and CNC-S/rGO, which exhibit high specific surface area, large pore volume, and well-developed mesoporosity, emerge as promising candidates for CDI electrodes. Notably, CNC-L/rGO incorporates longer carbon chains derived from long nanocellulose, which facilitates the formation of efficient conductive pathways within the material, thereby improving its electrochemical performance. Therefore, CNC-L/rGO was selected for further CDI testing compared to rGO. CNC-L strengthens the rGO structure by forming strong interactions with rGO sheets. At the same time, its well-dispersed fibers help maintain material integrity and prevent aggregation, resulting in improved mechanical stability and durability. Also, its larger pore size prevents rGO sheets from stacking too closely together, preserving a high surface area and facilitating efficient ion transport. This optimized structure enhances ion adsorption and release, which is essential for superior capacitive deionization (CDI) performance.

An asymmetric CDI configuration was constructed with rGO and CNC-L/rGO as the cathode for Na^+ capture and activated carbon (AC) as the anode for Cl^- capture. Compared to the symmetric CDI configuration, asymmetric CDI configurations exhibit enhanced desalination performance due to several advantages. These include the higher safe operation voltage (enabling operation at high voltage without inducing water splitting) and greater flexibility in the choice of electrode materials for Na^+ or Cl^- selectivity.

Fig. 6 illustrates the desalination performance of the samples studied at an initial NaCl concentration of 500 mg L^{-1} and operating voltage of 1.2 V, which is acceptable for asymmetric CDI cells. During the CDI process, no bubbles are observed, indicating the absence of side reactions, such as chlorine generation or water splitting. As shown in Fig. 6a and b, CNC-L/rGO demonstrates a high ion adsorption capacity (IAC) for Na^+ of 37.46 mg g^{-1} and a salt adsorption capacity (SAC) of 46.82 mg g^{-1}, significantly outperforming rGO, which has an IAC (Na^+) of 6.72 mg g^{-1} and SAC of 8.4 mg g^{-1}. Moreover, the CNC-L/rGO exhibits a higher IAR within 30 minutes (Fig. 6c). The corresponding CDI Ragone plots (Fig. 6d) show that CNC-

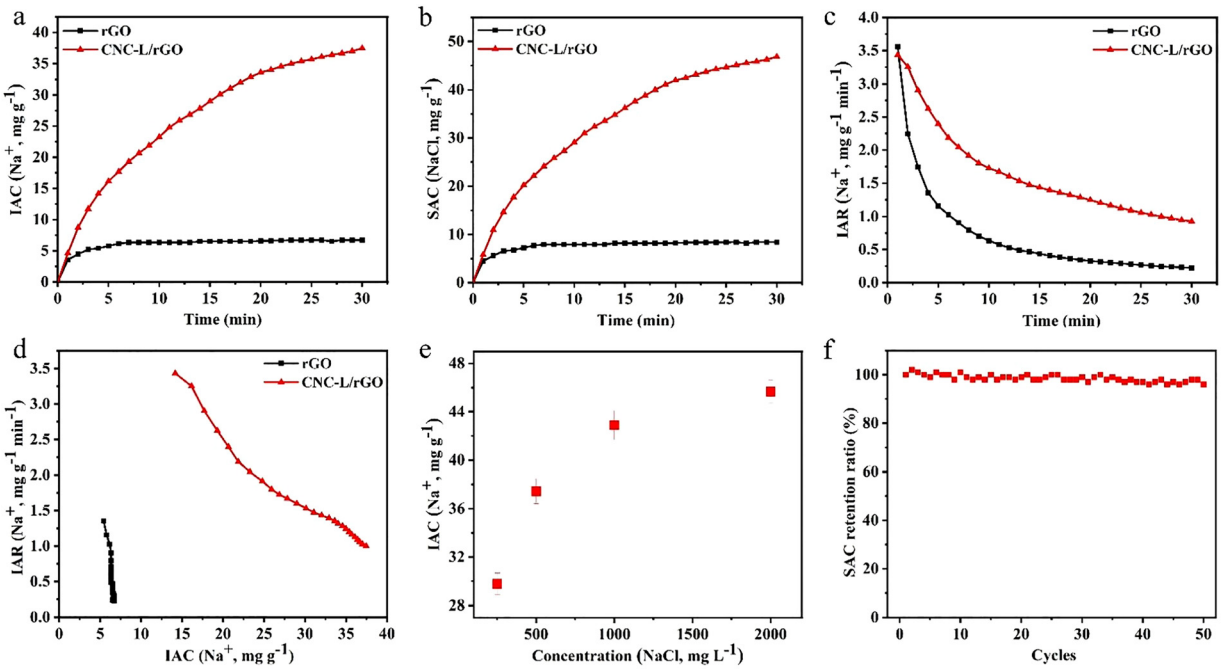

Fig. 6 CDI performance of rGO and CNC-L/rGO. (a) Ions adsorption capacity (IAC (Na^+)), (b) salt adsorption capacity (SAC (NaCl)), (c) ions adsorption rate (IAR (Na^+)) of the materials in 500 mg L^{-1} NaCl solution at 1.2 V, and (d) the corresponding Ragone plots for the materials in 500 mg L^{-1} NaCl solution at 1.2 V. (e) Sodium chloride concentration dependency of CDI performance for CNC-L/rGO at 1.2 V, (f) long-term cycling stability test of CNC-L/rGO in 500 mg L^{-1} NaCl solution at 1.2 V.

L/rGO shifts toward the upper right region, indicating higher IAC (Na^+) and faster IAR (Na^+) than rGO, due to large pore size and high surface area, which facilitates efficient ion adsorption and transport, critical for CDI performance.

For practical applications, the feedwaters used in CDI systems often consist of brines with varying concentrations. Therefore, achieving high CDI performance across a wide range of concentrations is crucial. The performance of CNC-L/rGO was further evaluated in NaCl solutions with concentrations ranging from 250 to 2000 mg L^{-1}. As the NaCl concentration increases, the Na^+ capture capacity also increases (Fig. 6e). Notably, CNC-L/rGO achieves an ultrahigh IAC (Na^+) of 45.67 mg g^{-1} at 2000 mg L^{-1}, along with a very high SAC of 57.08 mg g^{-1} (Table S1). Long-term cycling stability is another critical criterion for assessing practical CDI performance. The CNC-L/rGO nanocomposite was evaluated for stability at 1.2 V. Fig. 6f shows that the CNC-L/rGO nanocomposite exhibits excellent cycling stability, with no significant performance degradation even after 50 cycles. To further clarify the details of electrochemical Na^+ adsorption, *ex situ* X-ray photoelectron spectroscopy (XPS) measurements were carried out on the CNC-L/rGO sample before and after Na^+ adsorption.

As presented in Fig. S4a, the C 1s spectra of the as-prepared CNC-L/rGO electrode were deconvoluted into three peaks centered at approximately 290, 286, and 285 eV, corresponding to O–C═O, C–O, and C–C/C═C bonds, respectively.[50] After Na^+ adsorption (Fig. S4b), the O–C═O bond peak shifts toward lower binding energy, and the C–O bond peak shifts to higher binding energy, indicating redox activity related to these functional groups. Additionally, a new peak emerges at around 283 eV, attributable to Na–C interactions.[51] These findings align well with previously reported behaviors of sodium-ion interactions during charge/discharge processes.[52] Even after the CDI test, in the Raman spectra (Fig. S5a), the I_D/I_G ratio after CDI measurement remains almost unchanged (0.97), indicating that the defect density and graphitic ordering of the carbon framework are preserved during the cycling. This suggests that the conductive network remains intact under operating conditions. The wide-angle XRD results (Fig. S5b) further confirm the structural robustness of the material. Even after the CDI measurement, the (002) peak is still observed at 26.4°, with the calculated *d*-space remaining at 0.34 nm.

3. Conclusions

In summary, this study has successfully demonstrated nanocellulose-derived carbon/rGO nanocomposites using three distinct nanocellulose morphologies (CNF, CNC-L, and CNC-S), achieving enhanced surface areas exceeding between 170 and 283.9 m^2 g^{-1} due to the nanocellulose's role as a spacer preventing rGO restacking. CNC-L/rGO nanocomposite has demonstrated superior CDI performance, achieving a high IAC of 45.67 mg g^{-1} for Na^+ and an SAC of 57.08 mg g^{-1} at a NaCl concentration of 2000 mg L^{-1}. It also demonstrates excellent adaptability across saline concentrations (250–2000 mg L^{-1} NaCl) and long-term cycling stability over 50 cycles. These results highlight nanocellulose-derived carbon/rGO nanocomposite as a promising, scalable CDI material for efficient water desalination, paving the way for tailored designs to enhance desalination performance further.

4. Experimental section

4.1. Preparation of nanocellulose-derived carbon/rGO nanocomposites

Equal volumes of the above-prepared GO suspension and nanocellulose suspension (CNF, CNC-L, and CNC-S) were separately stirred in individual beakers. The GO suspension was then gradually added to the nanocellulose suspension under continuous stirring to form a binary suspension, with stirring maintained for an additional 20 minutes. The binary suspension was sonicated for 30 minutes and stirred magnetically for 24 hours. After these preparatory steps, the binary suspension was freeze-dried to obtain a dry nanocellulose/GO nanocomposite. This composite was then carbonized in a tube furnace at 600 °C for 8 hours with a temperature ramp of 5 °C min^{-1} under a nitrogen atmosphere to produce the nanocellulose-derived carbon/rGO nanocomposites. Once cooled to room temperature, the carbonized product was removed from the furnace and stored for subsequent use. The resulting samples were abbreviated as CNF/rGO, CNC-L/rGO, and CNC-S/rGO nanocomposites. For comparison, pristine rGO was prepared directly from GO under identical conditions without the addition of nanocellulose.

Conflicts of interest

There are no conflicts to declare.

Data availability

Data supporting this study are included within the article and/or supplementary information (SI). Supplementary information is available. See DOI: **https://doi.org/10.1039/d5nh00306g**.

Acknowledgements

This research was financially supported by the JST ERATO Yamauchi Materials Space-Tectonics Project (JPMJER2003) and the International Joint Research Project with Yonsei University (2023–2025). The authors acknowledge the contribution of Dugalunji Aboriginal Corporation on behalf of the Indjalandji-Dhidhanu people through the use of their equipment and in-kind support for the production of nanocellulose. Y. B. and S. M. A. appreciate the Distinguished Scientist Fellowship Program (DSFP) at King Saud University, Riyadh, Kingdom of Saudi Arabia, for the financial support. Additionally, a portion of this work was conducted at the Queensland node of the Australian National Fabrication Facility, an organization established under the National Collaborative Research

Infrastructure Strategy to provide nano- and microfabrication facilities for researchers across Australia. We also express our gratitude to English editing tools such as ChatGPT, Grammarly, and others, which assisted us in identifying and correcting grammatical errors in our manuscript.

References

1 T. Lu, Y. Liu, X. Xu, L. Pan, A. A. Alothman, J. Shapter, Y. Wang and Y. Yamauchi, *Sep. Purif. Technol.*, 2021, **256**, 117771.
2 Q. Li, X. Xu, J. Guo, J. P. Hill, H. Xu, L. Xiang, C. Li, Y. Yamauchi and Y. Mai, *Angew. Chem., Int. Ed.*, 2021, **60**, 26528–26534.
3 M. A. Anderson, A. L. Cudero and J. Palma, *Electrochim. Acta*, 2010, **55**, 3845–3856.
4 S. Dutta, S.-Y. Huang, C. Chen, J. E. Chen, Z. A. Alothman, Y. Yamauchi, C.-H. Hou and K. C.-W. Wu, *ACS Sustainable Chem. Eng.*, 2016, **4**, 1885–1893.
5 M. Elimelech and W. A. Phillip, *Science*, 2011, **333**, 712–717.
6 R. F. Service, *Science*, 2006, **313**, 1088–1090.
7 H. Deng, Z. Wang, M. Kim, Y. Yamauchi, S. J. Eichhorn, M. M. Titirici and L. Deng, *Nano Energy*, 2023, **117**, 108914.
8 C. L. Yeh, H. C. Hsi, K. C. Li and C. H. Hou, *Desalination*, 2015, **367**, 60–68.
9 S. Hu, D. Fang, F. Li, Z. Xu, K. Li, P. Zhang and W. Feng, *Desalination*, 2025, **601**, 118608.
10 D. Jiang, J. P. Hill, J. Henzie, H. N. Nam, Q. M. Phung, L. Zhu, J. Wang, W. Xia, Y. Zhao, Y. Kang, T. Asahi, R. Bu, X. Xu and Y. Yamauchi, *J. Am. Chem. Soc.*, 2025, **147**, 12460–12468.
11 Y. Li, Y. Wang, Y. Cai, R. Fang and L. Zhang, *Desalination*, 2024, **577**, 117387.
12 X. Xu, S. Zhang, J. Tang, L. Pan, M. Eguchi, J. Na and Y. Yamauchi, *EnergyChem*, 2020, **2**, 100043.
13 K. Laxman, L. Al Gharibi and J. Dutta, *Electrochim. Acta*, 2015, **176**, 420–425.
14 H. Wang, B. Chen, D.-J. Liu, X. Xu, L. Osmieri and Y. Yamauchi, *Small*, 2022, **18**, 2102477.
15 Q. Liu, S. Bi, X. Xu, X. Xiao and Y. Lei, *J. Colloid Interface Sci.*, 2025, **680**, 54–63.
16 H. M. Saif, B. Ferrández-Gómez, V. D. Alves, R. M. Huertas, G. Alemany-Molina, A. Viegas, E. Morallón, D. Cazorla-Amorós, J. G. Crespo and S. Pawlowski, *Desalination*, 2025, **602**, 118638.
17 Z. Liu, B. Wei, K. Liu and L. Wang, *Sep. Purif. Technol.*, 2024, **345**, 127380.
18 S. Zhang, Z. Ye, M. Ma, P. Yin, Y. Bao and F. Li, *Desalination*, 2025, **603**, 118679.
19 R. Patil, D. Jiang, X. Xu, N. Kumar, S. Bhattacharjee, S. K. Yadav, D. Kalyanasundaram, R. R. Salunkhe, A. Bhaumik, N. Khaorapapong, Y. Yamauchi and S. Dutta, *Chem. Eng. J.*, 2025, **506**, 159270.
20 C. Santos, E. García-Quismondo, J. Palma, M. A. Anderson and J. J. Lado, *Electrochim. Acta*, 2020, **330**, 135216.
21 H. Zhang, F. Zhang, Y. Wei, Q. Miao, A. Li, Y. Zhao, Y. Yuan, N. Jin and G. Li, *ACS Appl. Mater. Interfaces*, 2021, **13**, 21217–21230.
22 A. Ahmed, B. Adak, M. O. Faruk and S. Mukhopadhyay, *Ind. Eng. Chem. Res.*, 2021, **60**, 10882–10916.
23 H. Yang, H. Zheng, Y. Duan, T. Xu, H. Xie, H. Du and C. Si, *Int. J. Biol. Macromol.*, 2023, **253**, 126903.
24 A. Brakat and H. Zhu, *Nano-Micro Lett.*, 2021, **13**, 94.
25 J. Xing, P. Tao, Z. Wu, C. Xing, X. Liao and S. Nie, *Carbohydr. Polym.*, 2019, **207**, 447–459.
26 A. Brakat and H. Zhu, *ACS Appl. Bio Mater.*, 2021, **4**, 7366–7401.
27 S. Dutta, S.-Y. Huang, C. Chen, J. E. Chen, Z. A. Alothman, Y. Yamauchi, C.-H. Hou and K. C.-W. Wu, *ACS Sustainable Chem. Eng.*, 2016, **4**, 1885–1893.
28 D. Lin, Z. Zhou, R. Shi, B. Chen, Z. Huang, H. Tang, J. Wang, X. Zhu, C. Shao and F. Han, *J. Mater. Chem. A*, 2024, **12**, 19885–19890.
29 M. Tauk, G. Folaranmi, M. Cretin, M. Bechelany, P. Sistat, C. Zhang and F. Zaviska, *J. Environ. Chem. Eng.*, 2023, **11**, 111368.
30 N. Amiralian, M. Mustapic, M. S. A. Hossain, C. Wang, M. Konarova, J. Tang, J. Na, A. Khan and A. Rowan, *J. Hazard. Mater.*, 2020, **394**, 122571.
31 M. L. Pitcher, R. Koshani and A. Sheikhi, *J. Polym. Sci.*, 2024, **62**, 9–31.
32 G. Ramezani, T. G. M. van de Ven and I. Stihara, *Recent Prog. Mater.*, 2025, **7**, 1–65.
33 N. Amiralian, P. K. Annamalai, C. J. Garvey, E. Jiang, P. Memmott and D. J. Martin, *Cellulose*, 2017, **24**, 3753–3766.
34 F. V. Ferreira, M. Mariano, S. C. Rabelo, R. F. Gouveia and L. M. F. Lona, *Appl. Surf. Sci.*, 2018, **436**, 1113–1122.
35 R. J. Moon, A. Martini, J. Nairn, J. Simonsen and J. Youngblood, *Chem. Soc. Rev.*, 2011, **40**, 3941–3994.
36 K. Ge, H. Shao, E. Raymundo-Piñero, P. L. Taberna and P. Simon, *Nat. Commun.*, 2024, **15**, 1935.
37 M. A. Farea, N. Yusof, H. Y. Mohammed, M. N. Murshed, M. E. Al Sayed and D. Abdehameed, *Mater. Sci. Semicond. Process.*, 2025, **188**, 109219.
38 Y. Song, H. Lee, J. Ko, J. Ryu, M. Kim and D. Sohn, *Bull. Korean Chem. Soc.*, 2014, **35**, 2009–2012.
39 Abid, P. Sehrawat, S. S. Islam, P. Mishra and S. Ahmad, *Sci. Rep.*, 2018, **8**, 3537.
40 V. Paranthaman, K. Sundaramoorthy, B. Chandra, S. P. Muthu, P. Alagarsamy and R. Perumalsamy, *Phys. Status Solidi A*, 2018, **215**, 1800298.
41 I. Ahmed, R. Biswas, R. Sharma, V. Burman and K. K. Haldar, *Front. Chem.*, 2023, **11**, 1129133.
42 L. Zhu, Y. Cao, B. Jiang, J. Yu, J. Zhu and Z. Hu, *J. Alloys Compd.*, 2023, **969**, 172117.
43 D. López-Díaz, J. A. Delgado-Notario, V. Clericò, E. Diez, M. D. Merchán and M. M. Velázquez, *Coatings*, 2020, **10**, 524.
44 H. Liu, T. Xu, C. Cai, K. Liu, W. Liu, M. Zhang, H. Du, C. Si and K. Zhang, *Adv. Funct. Mater.*, 2022, **32**, 2113082.

45 V. T. Nguyen, L. Q. Ha, T. D. L. Nguyen, P. H. Ly, D. M. Nguyen and D. Hoang, *ACS Omega*, 2022, **7**, 1003–1013.
46 F. D'Acierno, W. Y. Hamad, C. A. Michal and M. J. Maclachlan, *Biomacromolecules*, 2020, **21**, 3374–3386.
47 M. Karakoti, R. Jangra, S. Pandey, P. S. Dhapola, S. Dhali, S. Mahendia, P. K. Singh and N. G. Sahoo, *High Perform. Polym.*, 2020, **32**, 175–182.
48 X. Sun, Z. Hao, X. Zhou, J. Chen and Y. Zhang, *Chemosphere*, 2024, **346**, 140601.
49 K. Sun, M. Tebyetekerwa, C. Wang, X. Wang, X. Zhang and X. S. Zhao, *Adv. Funct. Mater.*, 2023, **33**, 2213578.
50 R. Shu, L. Xu and Y. Guan, *J. Colloid Interface Sci.*, 2024, **675**, 401–410.
51 S. Aina, B. Tratnik, A. Vizintin, E. Tchernychova, M. P. Lobera, R. Dominko and M. Bernechea, *J. Power Sources*, 2024, **610**, 234730.
52 D. Jiang, R. Xu, L. Bai, J. P. Hill, J. Henzie, L. Zhu, W. Xia, R. Bu, Y. Zhao, Y. Kang, T. Hamada, R. Ma, N. Torad, J. Wang, T. Asahi, X. Xu and Y. Yamauchi, *Adv. Funct. Mater.*, 2024, **34**, 2407479.